JOURNAL OF MATERIALS SCIENCES 33 (1998) 4401–4415

Effect of martensitic transformation in Ti–15 at % V β-phase particles on lamellar boundary decohesion in γ-TiAl

Part II *Finite element analysis of crack-bridging phenomenon*

M. GRUJICIC, S. G. LAI
Program in Materials Science and Engineering, Department of Mechanical Engineering, 241 Flour Daniel Building, Clemson University, Clemson, SC 29634–0921, USA

The commercial finite element package ABAQUS has been used to analyse the crack bridging process by Ti-15 at % V β-phase particles dispersed in γ-TiAl matrix in the presence of particle–matrix decohesion. Both the particle–matrix decohesion potential and the β-phase materials constitutive relations are found to have a major effect on the ductility, fracture toughness and failure mode of the β–γ two-phase material. The interface potential is found to primarily affect the distribution of the normal interface strength ahead of the advancing interfacial crack and the mode (gradual versus sudden) of decohesion. The β-phase materials constitutive relations are found to influence the location of nucleation of the interfacial cracks and, in turn, the mode of decohesion. A metastable β-phase that can plastically deform at low stress levels by undergoing a stress-assisted martensitic transformation, but experience a high rate of strain hardening is found to give rise to the largest levels of ductility and fracture toughness is the β–γ two-phase material. © *1998 Kluwer Academic Publishers*

1. Introduction

There are a number of examples in the literature that demonstrate the potential for increasing the toughness of brittle solids by dispersing a ductile phase, [for example 1–3]. Two modes of toughening are established to be governed by the plasticity of the ductile phase:

1. Particles intercepted by the matrix crack, when bonded to the matrix, exhibit extensive plastic stretching in the crack wake [4] and cause toughness enhancement by inhibiting crack opening. When such a bridging zone exists, residual stresses present in the material, caused by thermal expansion mismatch, can also contribute to the toughness by means of its influence on the initial crack opening force.
2. Plastic deformation of particles in the region surrounding the crack gives rise to crack tip shielding [5].

In the case of the first mechanism, higher toughness levels are generally obtained for a large value of the product of the work of rupture for the particles and the particle size [6]. By contrast, crack shielding processes tend to become larger for ductile particles having small size and low yield strength [5].

Over the last two decades extensive experimental and computational research has demonstrated that deformation-induced martensitic transformation can lead to substantial enhancements in tensile ductility and fracture toughness of high–strength, brittle materials. The most significant improvements in materials tensile ductility and fracture toughness have been achieved in ZrO_2 and in various ceramics containing ZrO_2 second phase particles, e.g. Evans and Cannon [7], and in ultra-high strength secondary hardening steels, e.g. Olson [8]. In our recent study, Grujicic and Dang [9], found that the addition to the γ-TiAl intermetallic of 10 vol % of a metastable Ti–26Al–52V–5 Fe (wt %) body centred cubic (bcc) β-phase that undergoes a stress-assisted martensitic transformation gives rise to a nearly 100% increase in tensile ductility and in fracture toughness relative to the single phase γ-TiAl processed under identical conditions. A comprehensive experimental investigation of the fracture surface revealed that the observed enhancement in toughness and tensile ductility can be mainly attibuted to the crack-bridging effect of the β-phase particles located along the γ–γ lamellar boundaries accompanied by particle–matrix decohesion.

While the phenomenon of brittle-material toughening by particles of a ductile phase has been investigated extensively, the effect of metastable dispersed particles that can undergo a deformation-induced martensitic transformation has received considerably less attention. In particular, no report of crack bridging by transforming particles has been found in the literature. The effect of dispersed-phase martensitic transformation on crack shielding has been recently investigated by Grujicic and Sankavan [10, 11]. In the present work, crack-bridging by β-phase particles

undergoing a stress-assisted martensitic transformation and the accompanying particle–matrix decohesion process have been analysed within a continuum framework using the cohesion zone model initially developed by Needleman [12].

The fundamental basis for comprehending the phenomenon of martensitic transformation-enhanced toughness resides in the thermodynamics and associated kinetics of the deformation-induced transformation. The basic thermodynamics along with consideration of the pertinent martensitic nucleation and growth processes, permits descripton of the stress–strain characteristics of the transforming phase, which, in turn, allows determination of the crack-tip displacement and stress fields and, thus, quantification of the level of transformation enhanced toughness. Preliminary development of a materials constitutive model that takes into account the basic thermodynamic and kinetic aspects of stress-induced martensitic transformation in metastable β-phase particles embedded into a stable non-transforming matrix has been recently carried out by Grujicic and Sankaran [10]. The model takes into account the basic statistics of the heterogeneous martensitic nucleation process in dispersed systems as determined using the small particle martensitic transformation experiments of Cech and Turnbull [13]. Under the assumption of a random distribution of the orientation of the (pre-existing) nucleation sites, the effect of applied stress on the site potency and its distribution is evaluated and, in turn, the kinetics of stress-assisted martensitic transformation determined. The knowledge of the transformation kinetics is next used to determine the yield criterion and the flow rule for the evolving two phase (β phase + martensite) material. The results obtained by Grujicic and Sankaran [10] are used in the present work to develop a complete continuum materials constitutive model for the metastable β-phase.

Notation used in the present paper is based on the following conventions: Scalars are written in regular type (e.g.: f, γ, σ), vectors using bold face lowercase roman, (e.g., **e**, **t**), second-order tensors as bold face uppercase (e.g.: **T**, **D**), while fourth-order tensors use capital bold face italics (e.g.: ***I***, ***J***). Tensor (dyadic) products are indicated by '$\otimes$', tensor scalar products of appropriate order by a raised dot. The norm and the transpose of a second-order tensor **A** are denoted by $\| \mathbf{A} \|$ and $\mathbf{A}^{\mathbf{T}}$ respectively.

The organization of the paper is as follows: in Section 2.1., a brief description of the cohesive zone model used to describe the particle–matrix and matrix–matrix decohesion processes is given. Development of the material constitutive models for the β- and γ-phases is presented in Section 2.2. This is followed by a description of the finite element analysis of the particle crack-bridging process, Section 2.3. In Section 3, the results of the finite element analysis are presented and discussed. Main conclusions are drawn is Section 4. Derivation of the material Jacobian and its implementation in the displacement-based finite element program ABAQUS [14] are presented in the appendix.

2. Computational procedure

2.1. Interface cohesive zone model

The decohesion potential functions for the β-phase particle–γ-TiAl matrix interface and the γ–γ lamellar boundary of the type determined in Part I of this two-part paper [15], are incorporated in the finite element method to analyse large geometry changes encountered in the process of particle–matrix and matrix–matrix decohesion, from initial debonding until complete separation. The procedure for derivation of the constitutive relations for the β–γ and γ–γ interfacial elements and their incorporation into the commercial displacement-based finite element code ABAQUS [14] was previously given in the Appendix in Part I of this two-part paper [15].

The cohesive zone for both the particle–matrix and matrix–matrix interfaces is assumed to have negligible thickness, when compared to other characteristic lengths of the problem, such as the β-phase particle diameter, the computational domain size, typical lengths associated with the gradient of fields around the particle, etc. The mechanical behaviour of the interface is defined by the traction-displacement relations that are obtained by differentiating the interface potential, Φ, with respect to the normal and tangential interfacial displacements. Stable equilibrium for the interface is taken to correspond to a configuration associated with a minimum in the interface potential where all tractions vanish. For any other configuration, the value of the potential is taken to depend only on the interfacial displacement vector, **u**, Fig. 1. In the present work only axisymmetric deformation fields are considered and hence **u** is defined in terms of its normal component, u_n, and one tagential component, u_t, as

$$u_n = \mathbf{u}\,\mathbf{n} \tag{1}$$

$$u_t = \mathbf{u}\,\mathbf{t} \tag{2}$$

where **n** is the local normal to the interface, and **t** is the local tangent vector that lies in the r–z plane of the globl axisymmetric co-ordinate system.

Differentiation of $\Phi = \Phi(u_n, u_t)$ with respect to u_n and u_t yields, respectively, the normal, F_n, and tangential, F_t, components of the traction **F** per unit interface area in the deformed configuration

$$F_n(u_n, u_t) = \frac{-\partial\Phi(u_n,\ u_t)}{\partial u_n} \tag{3}$$

$$F_t(u_n, u_t) = \frac{-\partial\Phi(u_n,\ u_t)}{\partial u_t} \tag{4}$$

The interface constitutive relations are thus fully characterized by choosing a specific form for the decohesion potential. This is a major simplification of the actual interface behaviour, because, in general, the interfacial response may also depend on quantities such as displacement rate, local plastic deformation of the matrix and/or the particle, etc.

It is generally assumed that purely normal interface decohesion (tangential displacements, $u_t = u_b = 0$) the magnitude of F_n increases, reaches a maximum and

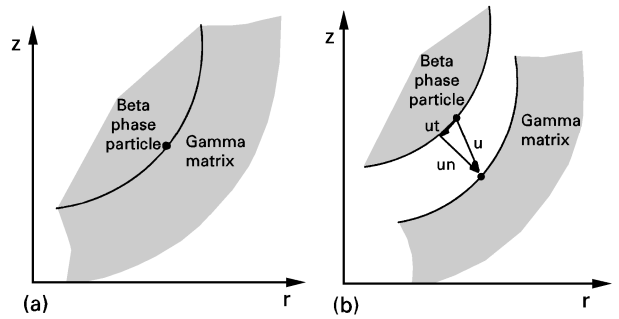

Figure 1 Interfacial displacement vector, **u**, and its normal, u_n, and shear, u_t, components in an axisymmetric deformation field of the β-phase particle and γ-phase matrix: (a) the reference configuration; (b) the configuration after decohesion.

then gradually falls to zero as complete interface separation occurs. This behaviour is confirmed by our atomistic simulation results obtained in Part I of this two-part paper [15]. The normal traction versus normal interfacial displacement relation obtained by differentiating the interface decohesion potential function shown in Fig. 11a in Part I [15] is plotted in Fig. 2a. The results shown in Fig. 2a, however, show that the behaviour of F_n at non-zero values of u_t and u_b is more complicated and even becomes negative at small values of u_n.

The shear behaviour of the particle–matrix interface is generally assumed to be non-periodic with F_t monotonically increasing with u_t until complete shear decohesion. The variation of F_t with u_t based on the interface potential function shown in Fig. 11b in Part I [15], which is plotted in Fig. 2b shows, however, that the shear response of the interface is periodic. These findings are consistent with the results of Bozzolo *et al.* [16] dealing with atomistic simulations of the ideal slip and interface sliding. In a parametric study of interfacial shear behaviour, Xu and Needleman [17] showed that for the limiting cases of very low or very high ratios of shear interfacial strength to normal interfacial strength, the couse of decohesion is fairly insensitive to whether the periodic or non-periodic shear behaviour of the interface is used. However, for intermediated regimes, the debonding process was found to depend significantly on the description of the interface shear response.

The pure normal decohesion behaviour of the interface is characterized in terms of its strength, σ_{max} (maximum value of F_n for $u_t = u_b = 0$), and the work of decohesion, $\Phi = \Phi(u_n \to \infty)$. σ_{max} is generally taken to be 1–2% of the matrix Young's modules (about two–four times the yield strength), while the work of decohesion is in the range of 1–10 J m^{-2}. Our results presented in Table II of Part I of this two-paper [15] fall into the range of values given above.

In the present work, the shear response of the interface is treated as periodic and of a friction-type so that a pure shear interface decohesion mode is not incorporated in the model. Rather, the effects of shear deformation are reflected in a periodic reduction of the capability of the interface to withstand normal decohesion. In other words, the peak normal strength is

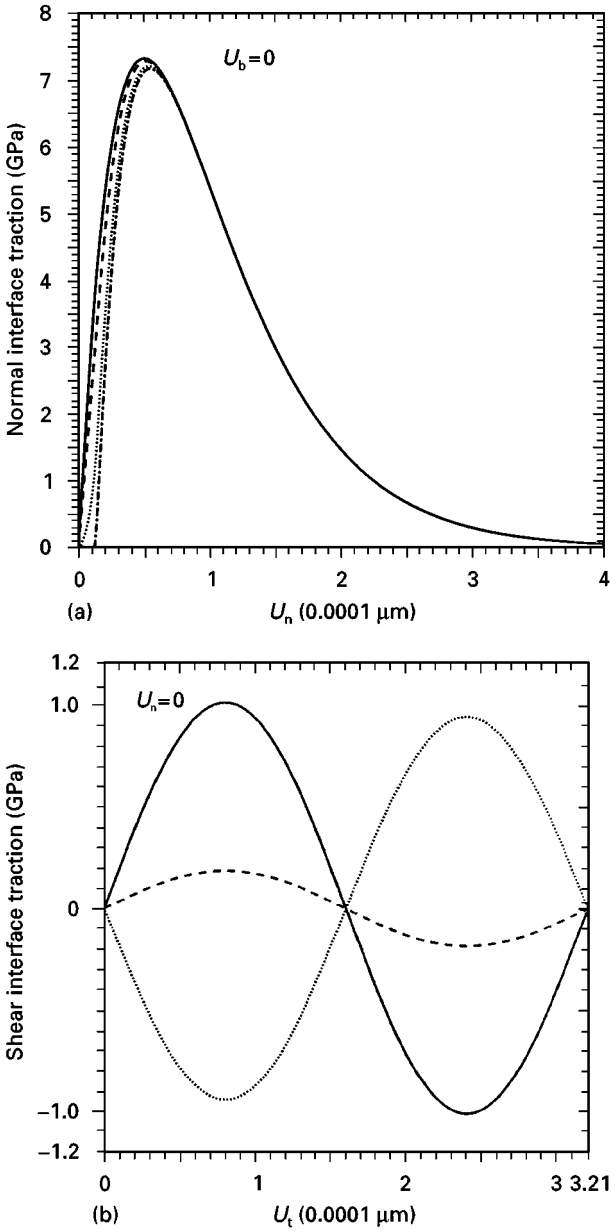

Figure 2 (a) Normal component of the traction per unit area of the $(1\,1\,0)_\beta/(1\,1\,1)_\gamma$ interface; (b) $[0\,0\,1]_\beta/[0\,\bar{1}\,1]_\gamma$ shear component of the traction for the same interface as in (a). u_n–$[1\,1\,0]_\beta/[1\,1\,1]_\gamma$ normal interface displacement, u_t and u_b are, respectively, $[0\,0\,1]_\beta/[0\,\bar{1}\,1]_\gamma$ and $[1\,\bar{1}\,0]_\beta/[2\,\bar{1}\,\bar{1}]_\gamma$ shear interface displacements. For (a) U_t: (—) 0 nm, (– –) 0.05 nm, (----) 0.1 nm, (— —) 0.15 nm. For (b) U_b: (——) 0 nm, (– –) 0.1 nm, (---) 0.2 nm.

a periodic function of the shear interfacial displacements.

The magnitude of the effective shear interfacial strength is generally not known and is therefore usual expressed as a fraction of the normal strength: $\tau_{max} = \alpha_t \sigma_{max}$, with $\alpha_t < 1$. The effect of different shear behaviours of the interface is assessed by varying the magnitude of the α_t parameter. The results shown in Table II, Part I of this two-part paper [15], show that in some cases τ_{max} can be larger than σ_{max} ($\alpha_t > 1$). This finding may not have a significant consequence because, based on the finite element results of Socrate [18], under high triaxiality fields that are used in the present work, the shear behaviour of the interface may not play a major role on the course of decohesion.

2.2. Materials constitutive relations

2.2.1. β-phase dispersion

In order to describe the constitutive law for a material completely, the appropriate equations must be given that define: (a) the stress–strain relationship; (b) the direction of plastic flow; (c) the yield criterion; and (d) the hardening rule. A preliminary derivation of these equations was carried out by Grujicic and Sankaran [10] using a thermodynamics, kinetics and mechanics-based analysis of transformation-controlled deformation in the dispersed phase of the two-phase system under consideration. A complete derivation of the materials constitutive relations is given below. The basic assumptions made in the present analysis are as follows:

1. The material inside the particles is initially composed entirely of the β-phase. A second phase, martensite, forms and its amount increases in the course of plastic deformation.
2. Each material point is assumed to contain the appropriate fractions of the two phases and the overall materials constitutive relation is a simple weighted averaged of the corresponding relations for the constituent phases.
3. Stress-assisted martensitic transformation and slip are the two plastic deformation modes taking place simultaneously in the β-phase, while martensite can undergo only plastic deformation by slip.
4. Both phases are elastically and plastically isotropic. The elastic properties of martensite are assumed to be equal to those of the β-phase.
5. Particles of the β-phase dispersed in the γ matrix do not interact with each other. They contain randomly oriented nucleation sites, and martensitic transformation proceeds by stress-assisted activation of these nucleation sites.
6. Strain and stress partitioning between the β-phase and the martensite is consistent with the Voigt upper bound model, which postulates that the strains in the two phases are equal.
7. The evolution of martensite, as well as evolution of the stresses, is assumed to be independent of the imposed strain-rate.

2.2.1.1. The stress–strain relationship. The stress–strain relationship is defined within a hypoelastic basis that is appropriate for large strain, rate-independent problems and the Kirchhoff stress **T**, is chosen as a suitable measure of the stress state. The relationship between the stress and the strain in rate form is given as

$$\overset{\nabla}{\mathbf{T}} = \boldsymbol{L}^e\,(\mathbf{D} - \mathbf{D}^{\mathrm{p}}) \tag{5}$$

where the Jaumann derivative of the Kirchhoff stress, $\overset{\nabla}{\mathbf{T}}$, and the fourth-order elasticity tensor, $\boldsymbol{L}^e$, are respectively, given as

$$\overset{\nabla}{\mathbf{T}} = \dot{\mathbf{T}} - \mathbf{W}\mathbf{T} + \mathbf{T}\mathbf{W} \tag{6}$$

and

$$\boldsymbol{L}^e = 2G\,(\boldsymbol{I} - \tfrac{1}{3}\,\mathbf{I}\otimes\mathbf{I}) + B(\mathbf{I}\otimes\mathbf{I}) \tag{7}$$

where $\dot{\mathbf{T}}$ is the material derivative of the Kirchhoff stress, **W** the spin tensor, G the elastic shear modulus, B the elastic bulk modulus, $\boldsymbol{I}$ the fourth-order identity tensor, and **I** the second-order identity tensor. **D** and $\mathbf{D}^{\mathrm{p}}$ in Equation 5 are the total stretching tensor and the plastic stretching tensor, respectively.

$\overset{\nabla}{\mathbf{T}}$ and $\boldsymbol{L}^e$ are defined using a weighted average of the corresponding quantities of the β-phase and martensite, as

$$\overset{\nabla}{\mathbf{T}} = f_\beta\,\overset{\nabla}{\mathbf{T}}_\beta + (1 - f_\beta)\,\overset{\nabla}{\mathbf{T}}_\alpha \tag{8}$$

and

$$\boldsymbol{L}^e = f_\beta\,\boldsymbol{L}^e_\beta + (1 - f_\beta)\,\boldsymbol{L}^e_\alpha \tag{9}$$

where β and α subscripts refer, respectively, to the β-phase and martensite and f_β and $(1 - f_\beta)$ are the volume fractions of the β-phase and martensite, respectively. Also, due to the use of the Voigt upper bound model, $\mathbf{D}^{\mathrm{p}} = \mathbf{D}^{\mathrm{p}}_\beta = \mathbf{D}^{\mathrm{p}}_\alpha$.

2.2.1.2. The yield criterion. By taking into account the effect of hydrostatic stress on the kinetics of martensitic transformation in the dispersed β-phase, Grujicic and Sankaran [10] defined the yield criterion for the two-phase material as

$$\tfrac{3}{2}^{1/2} \parallel \mathbf{T}' \parallel + \tfrac{1}{3} f_\beta\,\mathrm{ktr}\,(\mathbf{T}) \leqslant R\,(\bar{\varepsilon}) \tag{10}$$

where $\mathbf{T}'$ is the deviatoric Kirchhoff stress, k a (thermodynamic stability dependent) hydrostatic stress sensitivity parameter, tr stands for trace, R the yield resistance and $\bar{\varepsilon}$ the equivalent plastic strain. The yield resistance for the two-phase (β + martensite) material is defined by a weighted average of the yield resistances of the constitutent phase, R_β and R_α, as

$$R\,(\bar{\varepsilon}) = f_\beta\,R_\beta\,(\bar{\varepsilon}) + (1 - f_\beta)\,R_\alpha\,(\bar{\varepsilon}) \tag{11}$$

Due to the simultaneous operation of two deformation mechanisms, namely martensitic transformation and slip, the overall yield resistance of the β-phase, R_β is defined as

$$R_\beta\,(\bar{\varepsilon}_\beta) = 1/\frac{1}{R^{\mathrm{trans}}_\beta\,(\bar{\varepsilon}_\beta)} + \frac{1}{R^{\mathrm{slip}}_\beta\,(\bar{\varepsilon}_\beta)} \tag{12}$$

and R^{trans}_β and R^{slip}_β are, respectively, the yield resistances for the two deformation mechanisms.

A detailed analysis of the dispersed-phase martensitic transformation controlled deformation carried out by Grujicic and Sankaran [10], yielded the following expression for the transformation yield resistance:

$$R^{\mathrm{trans}}_\beta\,(\bar{\varepsilon}^{\mathrm{trans}}) = \frac{-2\;\beta}{V_{\mathrm{m}}\;[(\gamma_0^2 + \varepsilon_0^2)^{1/2} + \gamma_0)]} \left\{\frac{2\alpha\Gamma/\varrho}{\ln\,[1/-\,V_{\mathrm{p}} N^0_{\mathrm{v}}\;\ln\;(1 - \bar{\varepsilon}^{\mathrm{trans}}/\varepsilon_1)]} - \Delta g^{\mathrm{ch}} - g^{\mathrm{el}} - w_{\mathrm{f}}\right\} \tag{13}$$

where β is a β-phase chemical composition dependent constant, V_{m} is the molar volume, γ_0 and ε_0 are martensitic transformation normal and shear strains, α

is a nucleus potency distribution shape factor, Γ is the matrix–nucleus specific interfacial energy, ρ is the planar atomic density of the close packed crystal planes, V_p is the average volume of the martensite plate formed by activation of a single nucleation site, N_v^0 is the total number of nucleation sites per unit volume ε_1 is the equivalent plastic strain corresponding to the completion of martensitic transformation, Δg^{ch} is the chemical driving force for the transformation, g^{el} is the (coherent) elastic strain energy of the martensite nucleus, and w_f the frictional work of nucleus–matrix interfacial motion.

The slip resistance function for the β-phase, R_β^{slip}, and the yield resistance for martensite, R_α, are assumed to be consistent with power law hardening, i.e.

$$R_\beta^{slip}(\bar{\varepsilon}_\beta^{slip}) = K_\beta(\bar{\varepsilon}_\beta^{slip} + \varepsilon_\beta^*)^{n_\beta} \tag{14}$$

and

$$R_\alpha(\bar{\varepsilon}_\alpha) = K_\alpha(\bar{\varepsilon}_\alpha + \varepsilon_\alpha^*)^{n_\gamma} \tag{15}$$

where the parameters K_β, ε_β^*, n_β, K_α, ε_α^* and n_α are determined from the corresponding uniaxial tensile stress–strain data for the single β-phase and fully martensitic alloys.

2.2.1.3. The flow rule. The increment in the plastic strain tensor in the two-phase materials has been derived as

$$\Delta\varepsilon^p = \tfrac{3}{2}^{1/2}\,\dot{\bar{\varepsilon}}\Delta t\,\mathbf{N} + f_\beta\frac{\varepsilon_0 f\Delta t}{3}\mathbf{I} \tag{16}$$

where $\mathbf{N} = \mathbf{T}'/\|\mathbf{T}'\|$ is the deviatoric flow direction tensor, T' the deviatoric part of the Kirchhoff stress $\mathbf{T}$, $\dot{\bar{\varepsilon}}$ the equivalent plastic strain rate, and $\mathbf{f}$ the rate of increase of the volume fraction of martensite.

2.2.1.4. The hardening rule. The hardening rule, which essentially defines the tangent modulus that governs plastic flow of the two-phase material, is defined as

$$h(\bar{\varepsilon}) = \frac{dR(\bar{\varepsilon})}{d\bar{\varepsilon}} \tag{17}$$

where $R(\bar{\varepsilon})$ is given by Equations 11–15.

2.2.1.5. Integration of the material state. When a boundary value problem is being analysed using the finite element method, the knowledge of the material Jacobian for each Gaussian integration point at each time step is required to evaluate the elements stiffness matrix. A procedure for evaluation of the material Jacobian for the β-phase based on numerical integration of the material state is described below.

If the Kirchhoff stress tensor at time, t, is $\mathbf{T}_0$, the updated stress tensor at a new time step, $t + \Delta t$, is then given by

$$\mathbf{T} = \mathbf{T}_0 + \Delta\mathbf{T} \tag{18}$$

The increment in stress $\Delta\mathbf{T}$ can be defined as the integral of the Jaumann stress rate tensor and is given by

$$\Delta\mathbf{T} = \int_t^{t+\Delta t} \overset{\nabla}{\mathbf{T}}\,dt \tag{19}$$

Equation 19 can be evaluated using the generalized trapezoidal rule as

$$\Delta\mathbf{T} = \eta\overset{\nabla}{\mathbf{T}}\Delta t + (1-\eta)\overset{\nabla}{\mathbf{T}}_0\Delta t \qquad (0 \leqslant \eta \leqslant 1) \tag{20}$$

In the present work, η is set to one, which reduces the trapezoidal rule to the Euler backward difference method.

By combining Equations 18–20 and 5, the updated stress tensor can be expressed as

$$\mathbf{T} = \mathbf{T}_0 + \Delta t\,\boldsymbol{L}^e(\mathbf{D}) - \Delta t\,\boldsymbol{L}^e(\mathbf{D}^p) \tag{21}$$

After introducing the total strain increment

$$\Delta\varepsilon = \mathbf{D}\Delta t \tag{22a}$$

and the plastic strain increment

$$\Delta\varepsilon^p = \mathbf{D}^p\Delta t \tag{22b}$$

Equation 21 can be now rewritten as

$$\mathbf{T} = \mathbf{T}_0 + \boldsymbol{L}^e\,\Delta\varepsilon - \boldsymbol{L}^e\Delta\varepsilon^p \tag{23}$$

Because both the stress tensor from the previous time step, $\mathbf{T}_0$, and the total strain increment for the current time step, $\Delta\varepsilon$, are known, the first two terms on the right-hand side of Equation 23 are known. The third term is obtained by multiplying Equation 16 with Equation 7.

Combining Equations 23, 16 and 7, and taking advantage of the fact that $\mathbf{N}$ is purely deviatoric, so that $\mathbf{N}\cdot\mathbf{I} = \mathbf{0}$, yields

$$\mathbf{T} = \mathbf{T}_0 + \boldsymbol{L}^e\Delta\varepsilon - 6^{1/2}\,G\dot{\bar{\varepsilon}}\Delta t\mathbf{N} - Bf_\beta\varepsilon_0 f\Delta t\mathbf{I} \tag{24}$$

The $Bf_\beta\varepsilon_0\dot{f}\Delta t$ term represents a change in the hydrostatic stress due to the transformation volume change. This term is proportional to the equivalent transformation plastic strain increment in the β-phase, λ^{tarns}

$$Bf_\beta\varepsilon_0\dot{f}\Delta t = Bf_\beta\varepsilon_0\Delta f = Bf_\beta\varepsilon_0\frac{df}{d\bar{\varepsilon}^{trans}}\lambda^{trans} = \frac{Bf_\beta\,\varepsilon_0}{\varepsilon_1}\lambda^{trans} = b\lambda^{trans} \tag{25}$$

where the proportionality constant, b, is defined as $b \equiv Bf_\beta\varepsilon_0/\varepsilon_1$, and $df/d\bar{\varepsilon}^{trans}$ is set to $1/\varepsilon_1$ in accordance with the findings of Grujicic and Sankaran [10], that the equivalent transformation strain is a linear function of the transformed fraction of dispersed β-phase particles and that at the completion of martensitic transformation, when $f = 1$, the equivalent plastic transformation strain $\bar{\varepsilon} = \varepsilon_1$. The transformation plastic strain increment, λ^{trans}, is assumed to be related to the total equivalent plastic strain increment, $\lambda \equiv \dot{\bar{\varepsilon}}\Delta t$

$$\lambda^{trans} = \frac{h_\beta^{slip}}{h_\beta^{slip} + h_\beta^{trans}}\lambda \tag{26}$$

where h_β^{slip} and h_β^{trans} are the hardening rates obtained by differentiating R_β^{slip}, Equation 13, and R_β^{trans}, Equation 14, respectively, in accordanc with Equation 17. To simplify the computation, the $h_\beta^{slip}/(h_\beta^{slip} + h_\beta^{trans})$ term in Equation 26 can be assumed to be constant within a given time step and equal to its value at the beginning of the time step. Consequently Equation 24 can be written as

$$\mathbf{T} = \mathbf{T}_0 + \boldsymbol{L}^e \Delta\varepsilon - 6^{1/2} G\lambda \mathbf{N} - c\lambda \mathbf{I} \tag{27}$$

where c is a constant within the given time step.

The Kirchhoff stress given by Equation 27 can be further decomposed into its deviatoric component, $\mathbf{T}'$, and its hydrostatic component, $\frac{1}{3}\mathrm{tr}(\mathbf{T})\mathbf{I}$

$$\begin{aligned}\mathbf{T} &= \mathbf{T}' + \tfrac{1}{3}\,\mathrm{tr}\,(\mathbf{T})\mathbf{I} \\ &= \mathbf{T}'_0 + 2G\Delta\varepsilon' - 6^{1/2} G\lambda\mathbf{N} + \tfrac{1}{3}\mathrm{tr}(\mathbf{T_0})\,\mathbf{I} \\ &\quad + B\mathrm{tr}(\Delta\varepsilon)\mathbf{I} - c\lambda\mathbf{I}\end{aligned} \tag{28}$$

In accordance with Eqution 10, the yield condition is given as a linear function of the deviatoric and hydrostatic stresses

$$\tfrac{3}{2}^{1/2} \| \mathbf{T}' \| + \frac{f_\beta k}{3}\,\mathrm{tr}\,(\mathbf{T}) \leqslant R(\bar{\varepsilon}) = R(\bar{\varepsilon}_0 + \lambda) \tag{29}$$

where $R(\bar{\varepsilon})$ is the plastic flow resistance of the two-phase material at the current level of the effective plastic strai, $\bar{\varepsilon} = \bar{\varepsilon}_0 + \lambda$.

The stress is next updated using the radial return procedure introduced by Kreig and Kreig [19], which is based on the use of an elastic trial deviatoric stress

$$\mathbf{T}'_\mathbf{T} = \mathbf{T}'_\mathbf{0} + 2G\Delta\varepsilon' \tag{30}$$

and an elastic trial hydrostatic stress

$$\tfrac{1}{3}\,\mathrm{tr}\,(\mathbf{T_T})\mathbf{I} = \tfrac{1}{3}\,\mathrm{tr}\,(\mathbf{T_0})\mathbf{I} + B\,\mathrm{tr}(\Delta\varepsilon)\mathbf{I} \tag{31}$$

Next it is assumed that the updated deviatoric stress lies on the direction defined by $\mathbf{T}'_\mathbf{T}$, and the magnitude of both hydrostatic and deviatoric trial stresses relaxed in accordance with Equation 28 as

$$\| \mathbf{T}' \| = \| \mathbf{T}'_\mathbf{T} \| - 6^{1/2} G\lambda \tag{32}$$

$$\tfrac{1}{3}\,\mathrm{tr}\,(\mathbf{T}) = \tfrac{1}{3}\,\mathrm{tr}\,(\mathbf{T_T}) - c\lambda \tag{33}$$

until the yield criterion given by the equality in Equation 29 is satisified. By combining Equations 29, 32 and 33, the equilibrium condition can be expressed as the following non-linear algebraic equation

$$\begin{aligned}R(\bar{\varepsilon}_0 + \lambda) - \tfrac{3}{2}^{1/2}\,(\,\| \mathbf{T}'_\mathbf{T} \| - 6^{1/2}\,G\lambda) \\ - f_\beta k[\tfrac{1}{3}\,tr\,(\mathbf{T_T}) - c\lambda] = 0\end{aligned} \tag{34}$$

which can be readily solved for the unknown increment in the equivalent plastic strain, λ. Furthermore substitution of Equations 30–33 into Equation 28, yields the following expression for the updated stress

$$\begin{aligned}\mathbf{T} &= (\,\| \mathbf{T}' \|)\,\mathbf{N} + [\tfrac{1}{3}\,\mathrm{tr}\,(\mathbf{T})]\,\mathbf{I} \\ &= (\,\| \mathbf{T}'_\mathbf{0} + 2G\Delta\varepsilon \| - 6^{1/2} G\lambda)\,\mathbf{N} + [\tfrac{1}{3}\,\mathrm{tr}\,(\mathbf{T_0}) \\ &\quad + B\,\mathbf{tr}\,(\Delta\varepsilon) - c\,\lambda]\,\mathbf{I}\end{aligned} \tag{35}$$

The updated stess tensor, **T**, can hence be calculated by substituting the value for λ obtained as the solution of Eqution 34, into Equation 35. The updated stress tensor is used in the appendix to determine the material Jacobian.

2.2.2. γ-TiAl matrix

2.2.2.1. The stress–strain relationship. The rate form of the stress– strain relationship is given by an equation analogous to Equation 5, except that a subscript λ for the matrix phase should be used. The Jaumann derivative of the Kirchhoff stress. $\overset{\nabla}{\mathbf{T}}_\gamma$, and the fourth-order elasticity tensor for the γ-phase, $\boldsymbol{L}^e_\gamma$, are given by equations analogous to Equation 6 and 7, respectively.

2.2.2.2. The flow rule. Because the matrix phase undergoes a plastic deformation by slip but not by martensitic transformation, there is no accompanying volume change and hence the direction of the plastic flow should be set collinear with the deviatoric flow tensor $\mathbf{N}_\gamma = \mathbf{T}'_\gamma / \| \mathbf{T}'_\gamma \|$, and thus the plastic strain increment in the γ-phase can be defined as

$$\Delta\varepsilon^p_\gamma = \mathbf{D}^p_\gamma \Delta t = \tfrac{3}{2}^{1/2}\,\dot{\bar{\varepsilon}}_\gamma\,\Delta t\,\mathbf{N}_\gamma = \tfrac{3}{2}\,\Delta\bar{\varepsilon}_\gamma \mathbf{N}_\gamma \tag{36}$$

where $\Delta\bar{\varepsilon}_\gamma$ is the equivalent plastic strain in the matrix phase.

2.2.2.3. The yield condition. Because plastic flow in the γ-phase does not involve any volume change, a pressure independent yield condition such as the Von Mises yield criterion can be applied and the yield stress behaviour given by a parabolic function [20]

$$R_\gamma = K_\gamma\,(\bar{\varepsilon}_\gamma + \varepsilon^*_\gamma)^{n_\gamma} \tag{37}$$

2.2.2.4. The hardening rule. The rate of change in yield stress with the equivalent plastic strain can be defined by differentiating Equation 37 with respect to $\bar{\varepsilon}_\gamma$.

2.2.2.5. Integration of the material state. Due to the absence of pressure sensitivity of the yield stress and plastic incompressibility, this procedure is trivial and will not be discussed here.

2.3. Problem description

In the present work, finite element numerical simulations are carried out to analyse the crack-bridging process by dispersed β-phase particles in the presence of particle–matrix decohesion. A schematic of this process is given in Fig. 3a. All the simulations are done under the assumptions that the particles are precipitated along the γ–γ lamellar boundaries, that the cracks propagate along these boundaries and that the particles are subject to high triaxiality stress fields, characteristic of crack-tip regions. The numerical simulations are carried out to understand the effects of

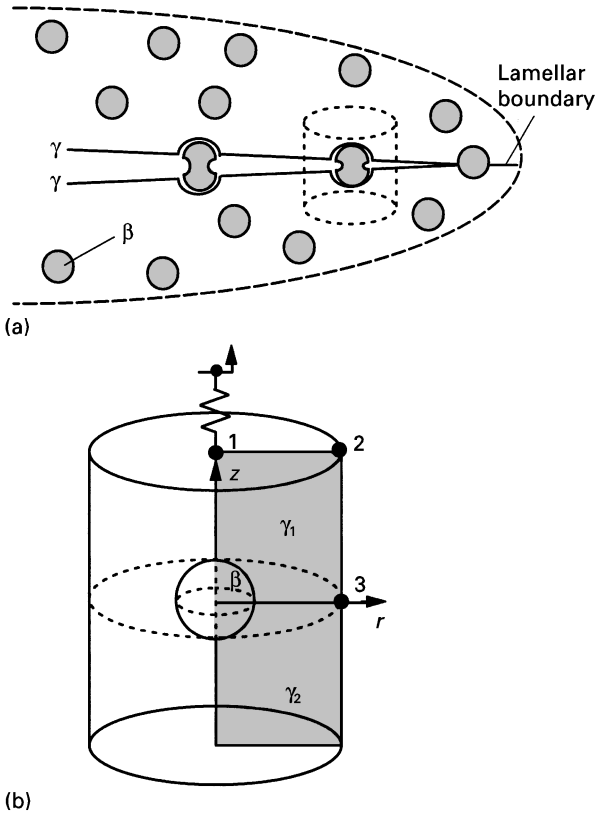

Figure 3 (a) Schematic representation of crack bridging in the presence of particle–matrix decohesion; (b) the axisymmetric cylinder containing an inclusion – the half of the inclusion is spheroidal, while the bottom half is an oblate ellipsoid; the shaded rectangle corresponds to the two-dimensional axisymmetric finite element mesh shown in Fig. 4. The spring and the special element composed of the nodes 1, 2 and 3 used to impose the constant triaxiality loading are also shown.

materials constitutive relations in the β-phase precipitates and the β–γ interface decohesion potential on the attainment of critical conditions for particle–matrix decohesion.

Because of the small length scales encountered in the present problem, some justification for the use of a continuum model is required. Typically, the β-phase particles precipitated along the γ–γ lamellar boundaries are about 1–10 μm in diameter [9]. On the other hand, the critical size of the martensite nucleation sites that might be found in these particles has been determined to be about 5.0 nm [21]. Thus the ratio of particle size to nucleation site size is, at least, of the order of 100 : 1. Also, transmission electron microscope observations of dislocation structure have shown [9] that the spacing of dislocations is much smaller than the particle diameter. It appears, therefore, that a continuum model is at least marginally justifiable.

Another concern regards the use of isotropic plasticity for the computational domain (the circular cylinder) that may lie within one γ-TiAl lamellar colony. A full three-dimensional analysis of decohesion, based on crystal plasticity, would certainly be more reliable. However, the primary objective of the present paper is to obtain a general understanding of the effect of martensitic transformation in the β-phase particles on crack bridging in the presence of particle–matrix decohesion under different loading conditions and the three-dimensional approach appears to be too costly to follow, because a drastic reduction in the scope of the parametric study would have to be used in order to compensate for the lengthy three-dimensional calculations. In addition, Xu and Needleman [17] showed that, under high triaxiality stress states, as is the present case, a considerable insight can be gained in the particle–matrix decohesion process by carrying a simplified isotropic plasticity analysis in place of the computationally more extensive crystal plasticity analysis.

As discussed in Part I of this two-part paper [15], a two-phase material containing discrete particles can be idealized as a uniform three-dimensional array of hexagonal cylinders of matrix material, each containing a spherical particle. This idealization is based on the assumption that all the particles are of the same shape, size and behave identically. Also, as discussed in Part I [15], the hexagonal cylinders can be replaced by circular cylinders. One of such circular cylinders can then be treated as a representative material element, Fig. 3b. The axisymmetric geometry of the circular cylinder requires axisymmetric loading and a "far-field" stress state that can be fully defined by specifying the levels of the applied axial and radial stresses, T_z and T_r. The orientation of the r-axis and z-axis in Fig. 3b is such that $T_z \geqslant T_r$, so that the far-field triaxiality parameter can be defined as

$$\Sigma = \frac{\frac{1}{3}\ \mathrm{tr} \parallel \mathbf{T} \parallel}{\frac{3}{2}^{1/2} \parallel \mathbf{T}' \parallel} = \frac{T_z + 2T_r}{3(T_z - T_r)} \tag{38}$$

To reduce the size of the computational domain, only one-quarter of the circular cylinder is generally analysed in the literature, for example [17]. This approximation promotes the model of particle decohesion that leaves the particle "floating" in the centre of the void at the completion of decohesion. This is not consistent with our experimental observations [9], which show that β-phase particles remain attached to the γ matrix after decohesion is complete. To prevent particle floating from occurring, the top half of the particle (along the positive z-axis) is taken to be spherical, with radius, r_t while the bottom hald (along the negative z-axis) is made to be an oblated ellipsoid of revolution with an aspect ratio of 0.9 (i.e. $r_b = 0.9\ r_t$, where r_b is the semiaxis of the ellipsoid in the z-direction). This geometry breaks the symmetry of the stress field around the particle, inducing slightly higher stress levels at the bottom of the particle and causes interface decohesion to occur earlier along the bottom of the particle. An effective radius for the particle, r_p, is then defined so that $V_p = (4/3)r_p^3$, where V_p is the volume of the particle. The sizes of the computational cylinder and the particle radius are chosen in such a way that the volume fraction of the β-phase is approximately 0.01.

Boundary conditions along the sides of the circular cylinder must meet the symmetry and periodicity conditions for modelling the infinite series of stacked circular cylinders. The cylinder is required to remain circular throughout the deformation history. Nodes

along the outer edge of the cylinder are constrained to have equal radial displacement; nodes along the top and the bottom of the cell are required to remain in planes normal to the z-axis; while nodes along the z-axis are constrained to have zero radial displacement. The loading conditions are prescribed by specifying the displacement rate in the axial direction for the top plane, while the nodes along the botton plane are constrained to move only in the radial direction. High triaxiality states are achieved by applying a negative pressure along the outer radius of the cylinder.

In order to keep the level of far-field triaxiality constant during the loading history, the radial stress, T_r, is defined via a distributed load (DLOAD) user-subroutine of ABAQUS that allows the user to scale T_r with the magnitude of axial stress, T_z. However, because the axial loading used is displacement controlled, the value of T_z is not known *a priori* and must be determined and made available to the DLOAD subroutine during the simulation runs. This was accomplished by using a three-node user-element and a stiff spring through which the axial displacement boundary conditions are applied to the cylinder, Fig. 3b.

Displacement-controlled loading is preferred to one in which stress boundary conditions are applied both in the axial and radial directions, because, for some combinations of the material and interface properties, equilibrium solutions may exist only if the far-field stress level decreases during the decohesion process. While the solution can be obtained under stress-controlled boundary conditions using a special solution algorithm, such as the modified Riks method, these algorithms are effective only if the response of the model is reasonably smooth. The latter may not be the case when the interface strength and decohesion potentials have low magnitudes.

Four-node isoparametric quadrilateral axisymmetric elements (CAX4) are used for both the β-phase particle and γ matrix, Fig. 4. These elements tend to lock, under the constraint of incompressible plastic flow, when the level of shear strain becomes very high (of order unity). In order to extend the analysis beyond this stage, alternative element formulations with reduced integration must be used. However, such elements may admit deformation modes that cause no straining at the integration points. These zero-energy modes make the element rank-deficient, and cause a phenomenon known as "hourglassing", in which zero-energy modes propagate through the mesh, leading to inaccurate solutions. To prevent hourglassing, an additional artificial stiffness is added to each element. For the boundary value problem under consideration, due to the large values of shear deformation encountered in the region near the interface, the tendency toward hourglassing is highly pronounced so that a large hourglass stiffness must be used, which as shown by Socrate [18] can significantly alter the solution. For these reasons, full-integration CAX4 elements are used in the present analyses. The β–γ interface and γ–γ lamellar boundary are modelled using the interfacial elements whose constitutive relations are derived using the procedure described in the appendix of Part I of this two-part paper [15].

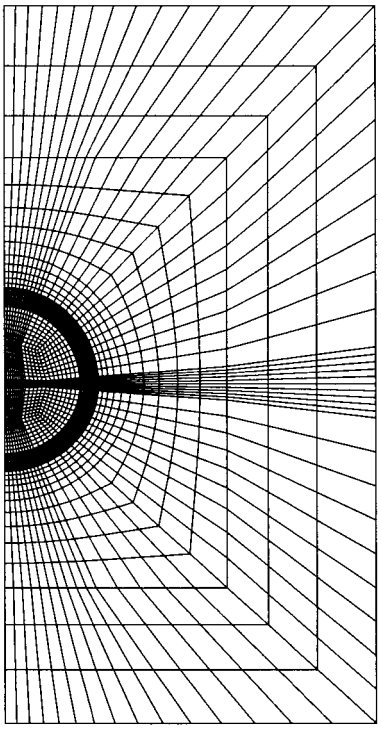

Figure 4 Axisymmetric finite element mesh used in the present work.

In order to carry out the analysis of crack bridging in the presence of interface decohesion, a number of parameters can be varied such as those that describe:

- interface behaviour,
- constitutive behaviour of the particle phase,
- constitutive behaviour of the matrix phase,
- loading conditions, and
- cylinder geometry, etc.

An all-inclusive analysis, in which each of these parameters are independently varied within a relevant range, is not carried out in the present work. Rather, the investigation is divided into two sets of parametric studies. In the first study the effects of varying interface properties within the range observed in Part I [15] and loading conditions on crack-bridging phenomenon are considered. In the second study, the loading conditions and the interface properties are fixed, and the effect of varying β-phase materials constitutive relations is investigated.

3. Results and discussion

3.1. The effect of β–γ interface decohesion potential

In this set of calculations, the constitutive relations for the β-phase are fixed and set equal to the ones that were shown by Grujicic and Sankaran [11] to give rise to the maximum crack-tip shielding effect in γ-TiAl. The constitutive relations for martensite and γ-Tial as determined by Grujicic and Sankaran [11] are also used in the present calculations. The values of materials parameters for the three phases (β, martensite and

TABLE I Values of the constitutive model parameters used in the analysis of the γ-TiAl–β-Ti–Al–V–Fe system

Parameter	Value	Used in equation number	Reference
B_β, GPa	58	7	[10]
G_β, GPa	27	7	[10]
B_γ, GPa	133	7	[10]
G_γ, GPa	62	7	[10]
k	1.2	10	[10]
β	2.73	13	[10]
γ_0	0.08	13	[10]
ε_0	0.04	13	[10]
α	0.84	13	[10]
Γ J m^{-2}	0.15	13	[10]
ρ mol m^{-2}	3.01×10^{-5}	13	[10]
N_v^0	2×10^{17}	13	[10]
V_p, m^3	10^{-14}	13	[10]
$g^{el} + w_f$, J mol^{-1}	180	13	[10]
ε_1	0.048	13	[10]
K_β, MPa	1385	14	[22]
ε_β	8.88×10^{-4}	14	[22]
n_β	0.145	14	[22]
K_α, MPa	1302	15	[22]
ε_α	9.04×10^{-3}	15	[22]
n_α	0.135	15	[22]
K_γ, MPa	1310	37	[20]
ε_γ^*	2.12×10^{-2}	37	[20]
n_γ	0.128	37	[20]

γ-TiAl) used in the present work are give in Table I. The γ–γ lamellar boundary decohesion potential is set equal to the one determined in Part I of this two-part paper [15]. The complete form of the β–γ interface decohesion potential derived in Part I [15] is not used in the present work. Rather, the results obtained in Part I are used to define the bounding values of the parameters appearing in the interface potential function. Specifically, to comply with the axisymmetric character of the computational model used, the shear behaviour of the interface is assumed to be independent of the direction of shear. In addition, the shear and normal decohesion behaviours of the β–γ interface are assumed to be independent of the orientation of the interface. The results given in Table II of Part I [15] justify this assumption relative to the normal interface behaviour but not relative to the shear behaviour. To overcome this limitation, the effect of the magnitude of the shear interfacial strength within the range identified in Part I is explored Specifically, three cases of β–γ interfacial decohesion potentials are analysed. In all cases the work of decohesion and the normal interfacial strength are set to $\Phi(u_n \to \infty) = 2$ J m^{-2} and $\sigma_{max} = 6$ GPa, respectively, while the shear strength is varied as: case I, $\tau_{max} = 0.6$ GPa; case II, $\tau_{max} = 6$ GPa; and case III, $\tau_{max} = 40$ GPa. All the calculations are done under the applied triaxiality of $\Sigma = 2.4$, which corresponds to the value predicted gy the Prandtl slip-line field approach $\Sigma = (1 + \pi)/3^{1/2}$ [18].

The relationship between the axial stress and the axial displacement of the computational cylinder for the three cases of β–γ interface decohesion potential is shown in Fig. 5. In all three cases the axial stress

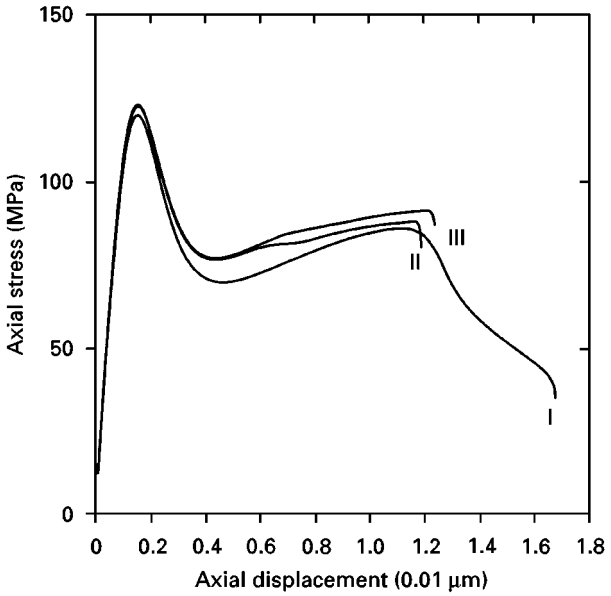

Figure 5 The relationship between the axial stress and the axial displacement of the top surface of the computational cylinder shown in Fig. 3(b). The three curves correspond to different values of the normal and shear strength of the β–γ interface as follows: I $\sigma_{max} = 6$ GPa, $\tau_{max} = 0.6$ GPa; II $\sigma_{max} = 6$ GPa; $\tau_{max} = 6$ GPa; III $\sigma_{max} = 6$ GPa, $\tau_{max} = 40$ GPa.

initially increases very fast until a peak value is reached at which γ–γ lamellar boundary separation takes place and consequently a stress drop occurs. The stress drops to about two-thirds–one-half of its peak value and then begins to recover at a very slow rate. The second drop in stress is associated with decohesion along the β–γ interface and results in fracture of the specimen.

The variation of normal and shear displacements along the β–γ interface for the three cases of β–γ interface potential is shown in Fig. 6. These displacements are used to determine the variation of the local normal interface strength (local normal interface strength is dependent on the local shear displacement) along the β–γ interface and to identify the portion of the interface that has undergone decohesion (the portion of the interface where the local normal displacement is greater than its value at the normal stress level equal to the local normal interface strength). The results of this procedure are shown in Fig. 7. The section of the interface that has undergone decohesion is designated as "debonded".

The contour plots of the martensite volume per cent, f (%), per cent equivalent plastic strain $\bar{\varepsilon}^{pl}$ (%), and the radial, T_r, and axial, T_z, stresses for cases I and II of the β–γ interface potential are shown, respectively, in Figs 8 and 9. The contour plots for case III are very similar to the corresponding contour plots for case II and hence are not shown. To improve the clairty of the contour plots only the innermost region of the computational domain surrounding the β–γ inferface and the γ–γ lamellar boundary junction is displayed in Figs 8 and 9. In addition to showing contours of the aforementioned quantities, Figs 8 and 9 also show the mode of the β–γ interface decohesion. For all three cases of β–γ interface potential, decohesion starts in the region where the γ–γ

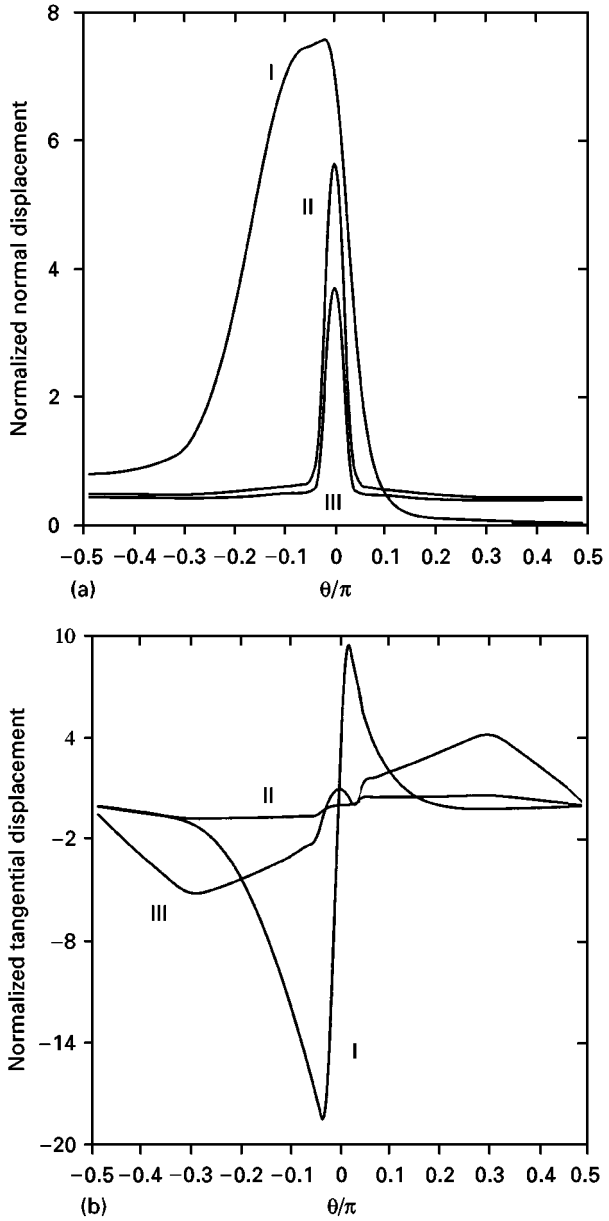

Figure 6 Distribution of normal (a) and tangential (b) displacements along the β–γ interface before complete decohesion takes place. The displacements are normalized with respect to the characteristic normal and shear interface separation distances, δ_n and λ_t, respectively. See Fig. 5 for the explanation of symbols I, II and III. Theta is the radial angle.

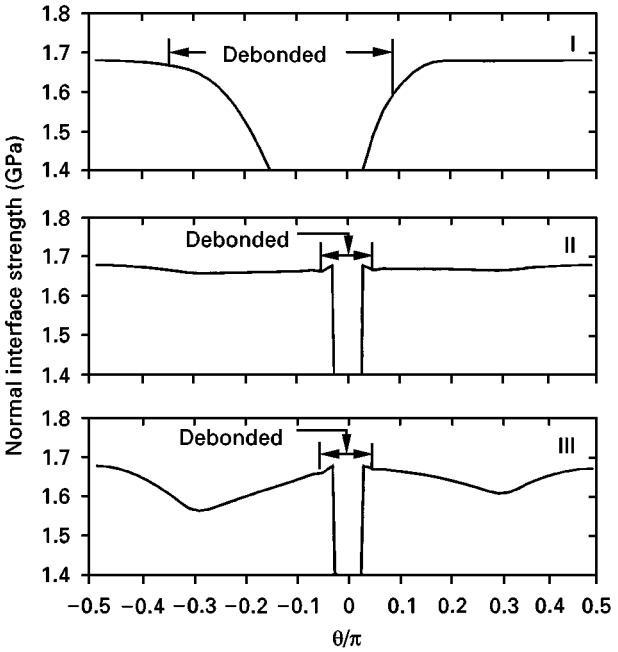

Figure 7 Variation of normal interface strength along the β–γ interface before complete decohesion takes place. The portions of the interface where the normal displacement exceeds the local characteristic normal separation distance, δ_n, is marked as "debonded". See Fig. 5 for the explanation of symbols I, II and III.

lamellar boundary impinges on the β-phase particle (the polar angle $\theta \approx 0$) and then spreads along the β–γ interface. Initially the spread takes place both in positive and negative θ directions. However, final debonding always takes place along the lower (negative θ) portion of the interface.

The results shown in Figs 5–9 can be summarized as following:

1. The location of the initial β–γ interface crack is not affected by the magnitude of the shear interface strength. That is, for all three cases analysed the crack nucleates in the region where the γ–γ lamellar boundary touches the β-phase particle, Figs 8 and 9.

2. The final fracture occurs by crack propagation along the lower half of the β-phase particle for all three cases studied.

3. The total strain to fracture, Fig. 5, is affected by the magnitude of the shear interface strength and is larger by 30–35% for the case when $\sigma_{max} > \tau_{max}$, case I, than for the other two cases.

4. Fracture toughness, which is proportional to the area under the stress–displacement curves in Fig. 5, is also larger by 30–35% in case I relative to the other two cases.

5. The final fracture is relatively gradual in case I and quite abrupt in cases II and III, Fig. 5. This appears to be related to differences in the distribution of the normal interface strength in front of the interface crack, Fig. 7. In case I, Fig. 7, the normal interface strength increases with distance from the crack tip and this ensures a more stable mode of crack propagation. In sharp contrast, in cases II and III, the normal interface strength decreases with distance from the crack tip and this causes unstable crack propagation and abrupt fracture.

6. The β-phase particle can undergo a significant amount of plastic deformation before final debonding and similarities in the martensite volume fraction and equivalent plastic strain fields indicate that plastic deformation is dominated by martensitic transformation, Figs 8 and 9.

7. A smaller shear interface strength, case I, promotes a more uniform distribution of plastic strain in the β-phase, Fig. 8 relative to cases II and III, Fig. 9. These differences may also contribute to the mode (gradual versus abrupt) of fracture.

8. The stresses acting on the lower half of the β–γ interface are consistently higher (e.g. T_z in Fig. 8) and this appears to be the reason that final fracture always takes place along this portion of the interface.

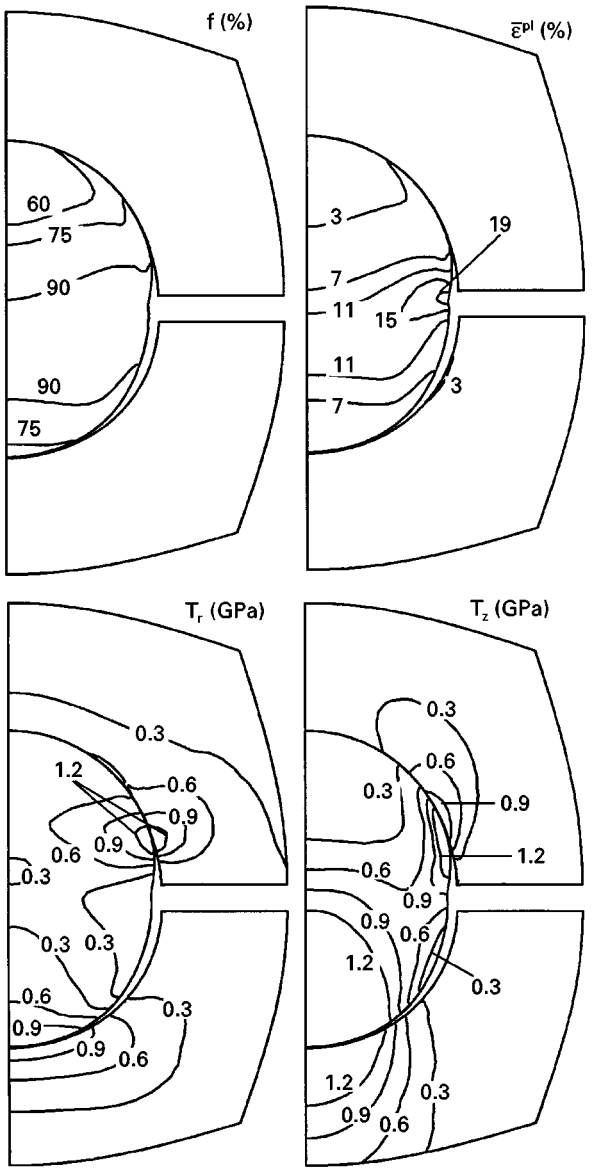

Figure 8 Contour plots for the volume per cent of martensite (a) per cent equivalent plastic strain (b), radial stress (c), and axial stress (d) for case I of the β–γ interface potential.

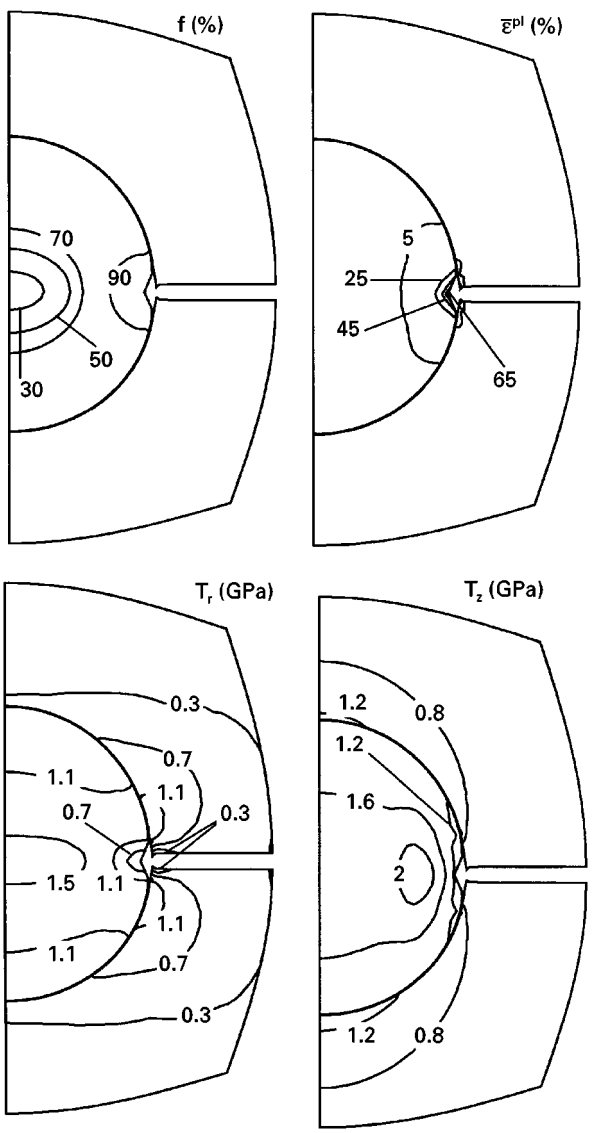

Figure 9 Contour plots for the volume per cent of martensite, (a) per cent equivalent plastic strain (b), radial stress (c), and axial stress (d) for case II of the β–γ interface potential.

3.2. The effect of β-phase thermodynamic stability

In this set of calculations, the materials constitutive properties for γ-TiAl and martensite, the γ–γ lamellar boundary decohesion potential and the applied triaxiality are all kept equal to their values used in Section 3.1. The β–γ interface decohesion potential is set equal to case I in Section 3.1, i.e. $\sigma_{max} = 6$ GPa and $\tau_{max} = 0.6$ GPa. The material constitutive relations for the β-phase have been varied by setting the magnitude of the chemical driving force for $\beta \rightarrow$ martensite martensitic transformation, Δg^{ch}, to the following three values: case A: $\Delta g^{ch} = 0$ J mol^{-1}; case B: $\Delta g^{ch} = 900$ J mol^{-1} and case C: $\Delta g^{ch} = 1800$ J mol^{-1}. The three cases of the β-phase correspond to three different levels of β-phase thermodynamic stability as follows: Case A: the β-phase possesses a high level of stability so that it does not undergo any transformation to martensite. Case B: this β-phase is, in fact, the one used in Section 3.1. that can undergo martensitic transformation during loading. Case C corresponds to the unstable β-phase that transforms fully to martensite before any loading is applied. In addition to these three cases, case D pertaining to the β-phase with a low initial yield stress (equal to that of the β-phase in case B) and a low rate of strain hardening (same as that of the β-phase in case A) is analysed. Case D is studied in order to separate the effects of initial yield stress and rate of strain hardening on crack bridging and interface decohesion.

The relationship between the axial stress and the axial displacement for the four cases of the β-phase materials constitutive relation is shown in Fig. 10. The distribution of the normal and shear displacement along the β–γ interface and the corresponding variation of the local normal interface strength are shown in Figs 11 and 12, respectively. The contour plots for the per cent equivalent plastic strain, and the radial and axial stresses for cases A and D are shown in Figs 13 and 14, respectively. The corresponding contour plots for Case B are shown in Fig. 8 (case I), while the ones for case C are similar to their counterparts in case A and are not shown for brevity.

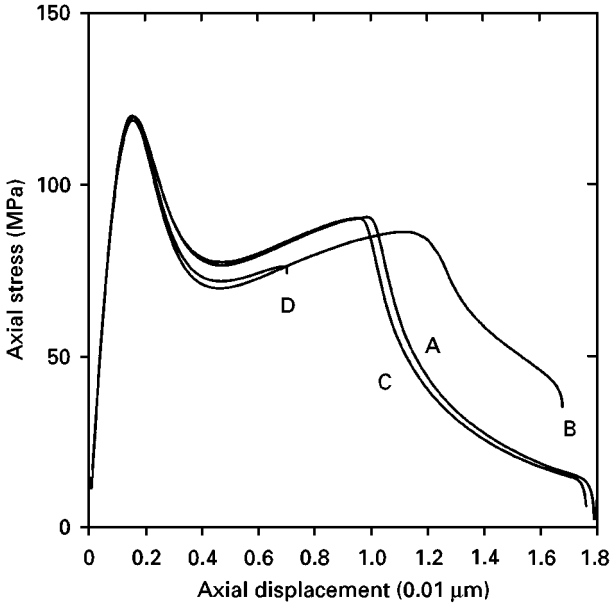

Figure 10 The relationship between the axial stress and the axial displacement of the top surface of the computational cylinder shown in Fig. 3b. The four curves correspond to different materials constitutive relations for the β-phase. See text for details.

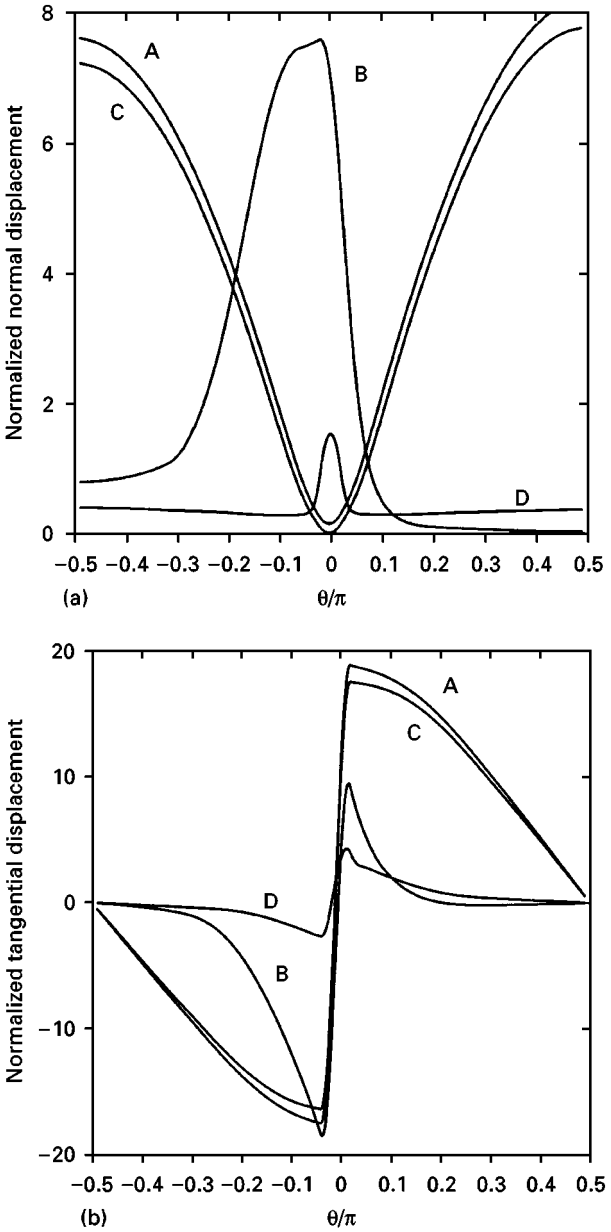

Figure 11 Distribution of normal (a) and tangential (b) displacements along the β − γ interface before complete decohesion takes place. The displacements are normalized with respect to the characteristic normal and shear interface separation distance, δ_n and λ_t, respectively. See text for the explanation of symbols A, B, C and D.

The results shown in Figs 10–14 can be summarized as follows:

1. Both ductility and fracture toughness are affected by the constitutive relation for the β-phase particle, Fig. 10. The case of the metastable β-phase that can undergo a stress-assisted martensite transformation, case B, yields the highest level of fracture toughness and a high level of ductility.

2. The location of nucleation of the interface crack is affected by the β-phase constitutive relations, i.e. thermodynamic stability. For cases A and C, Fig. 13, which are characterized by a relatively high yield stress of the β-phase, the crack nucleates at the lowest part ($\theta \simeq -\pi/2$) of the β–γ interface and continues to propagate upwards during subsequent loading. Contrary, for cases B and D in which the initial yield stress is relatively small the crack nucleates in the region where the γ–γ lamellar boundary touches the β-phase particle ($\theta \approx 0$).

3. In cases A and C in which crack nucleation takes place at the lower part of the β–γ interface, Fig. 13, the Poisson's effect in the γ matrix opposes interface decohesion. This appears to be the main reason for the slightly higher ductility levels obtained in these cases, Fig. 10. Fig. 12 suggests that the decohesion process is relatively stable in this case due to slightly higher normal interface strength values ahead of the interface crack.

4. The metastable β-phase, case B, undergoes a considerably higher amount of plastic deformation, Fig. 8, than the stable or unstable β-phases, case A and C, Fig. 13. This behaviour appears to be caused by the lower values of the yield stress in case B.

5. For the β-phase characterized by the smallest magnitudes of yield stress and rate of strain hardening, case D, the results shown in Fig. 10 suggest the lowest values of materials ductility and fracture toughness. However, the "failure" in Fig. 10 is due to numerical difficulties encountered during the calculation rather than due to final interface debonding. These difficulties are the result of a large gradient of the equivalent plastic strain in the β-phase near the interface crack, which leads to severe distortions in the corresponding elements, Fig. 14. A comparison of the T_r and T_z values near the crack tips in Fig. 14 with the normal interface strength profile, Fig. 12, shows that the condition for further crack growth are not met prior to "failure", which further confirms that final debonding does not take place. The issue of numerical problems due to excessive mesh distortion has not been dealt with in the present work. However, when the mesh size is refined by doubling the number of elements in the region surrounding the interface crack it is found that the "failure" is slightly delayed. However, due to

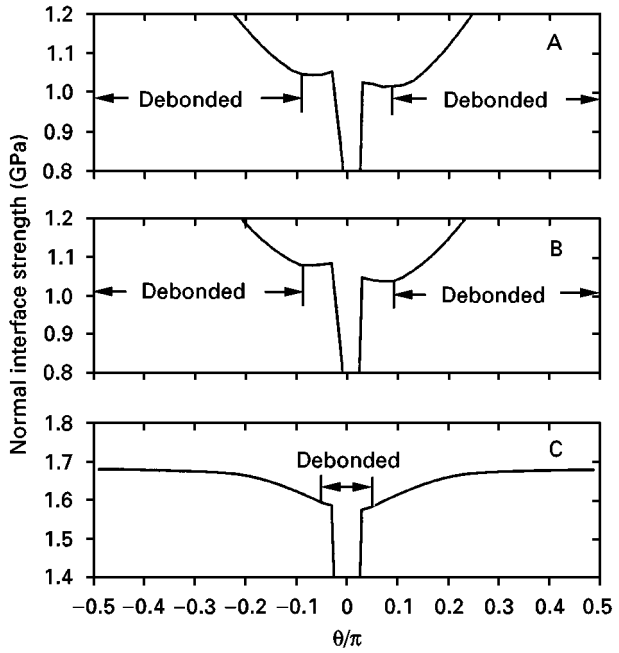

Figure 12 Variation of normal interface strength along the β–γ interface before complete decohesion takes place. The portions of the interface where the normal displaement exceeds the local characteristic normal separation distance, δ_n, is marked as "debonded". See text for the explanation of symbols A, B and C.

a small rate of strain hardening, plastic deformation in the β-phase remained localized in the neck region ($z \approx 0$), which would ultimately lead to rupture of the β-phase particle. To model the rupture process, a failure criterion would have to be incorporated into simulations. Because such a criterion is not available for the β-phase corresponding to case D, and the issue of excessive distortions of the elements is not dealt with, particle rupture was not analysed in the present work. Nevertheless, in case D, true failure is expected to involve rupture and the β-phase particle. Consequently, higher ductility of the β-phase would give rise to higher ductility levels in the two-phase β–γ material. However, due to the low rate of strain hardening of the β-phase in case D, fracture toughness of the two-phase material may not be as high as in the case of the metastable β-phase, case B.

4. Conclusions

Based on the results obtained in the present work the following two main conclusions can be drawn:

1. For a constant value of the β-phase particle–γ-TiAl matrix work of decohesion and fixed β-phase and γ-TiAl materials constitutive relations, the relative magnitude of the normal and shear interface strengths (within the range suggested by our atomistic simulation work) does not affect the place where the initial β-phase particle–γ matrix interface crack forms. However, the crack growth rate and plastic deformation of the material surrounding the crack, and consequently the materials ductility and fracture toughness are significantly affected by the relative magnitude of the two interface strengths. Specifically, when the shear strength is lower than the normal one the ductility and toughness achieve the largest values.

2. The thermodynamic-stability controlled constitutive relations for the β-phase affect the place where the initial crack forms, subsequent crack growth and evolution of the surrounding material and, in turn, the levels of materials ductility and toughness. The highest levels of ductility and toughness are achieved in the case when the initial yield stress of the β-phase is relatively small while its rate of strain hardening is

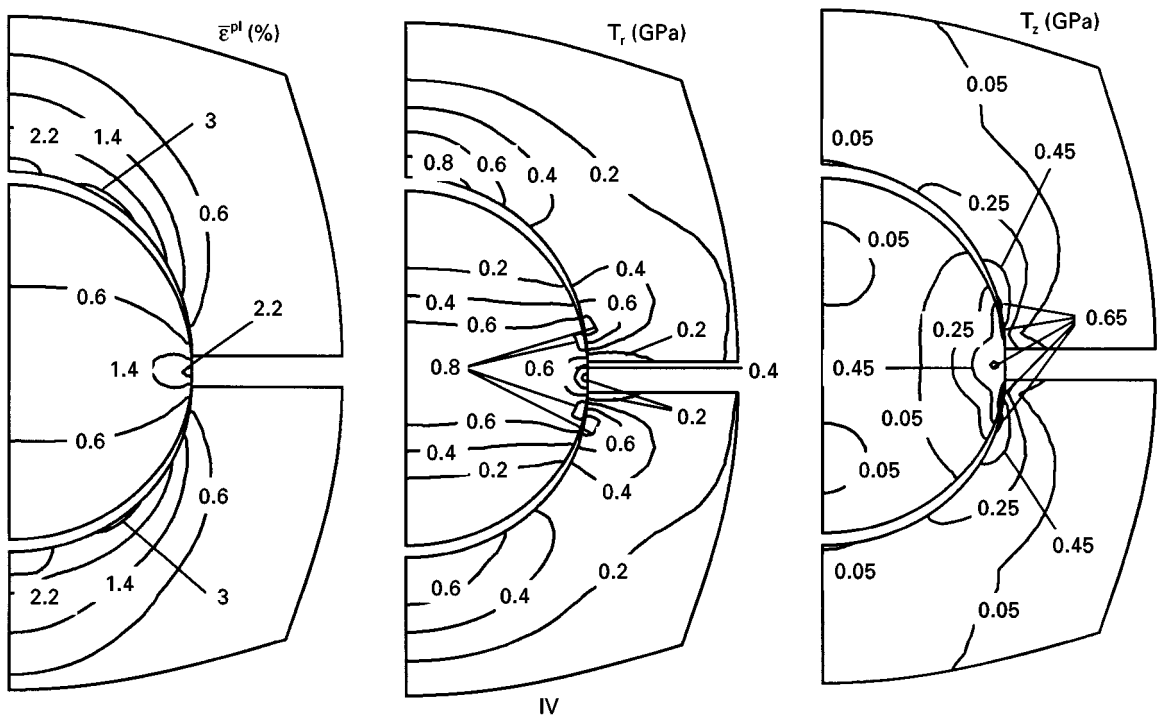

Figure 13 Contour plots of the per cent equivalent plastic strain, (a), radial (b), and axial stress (c), for case A of the β-phase material constitutive relation.

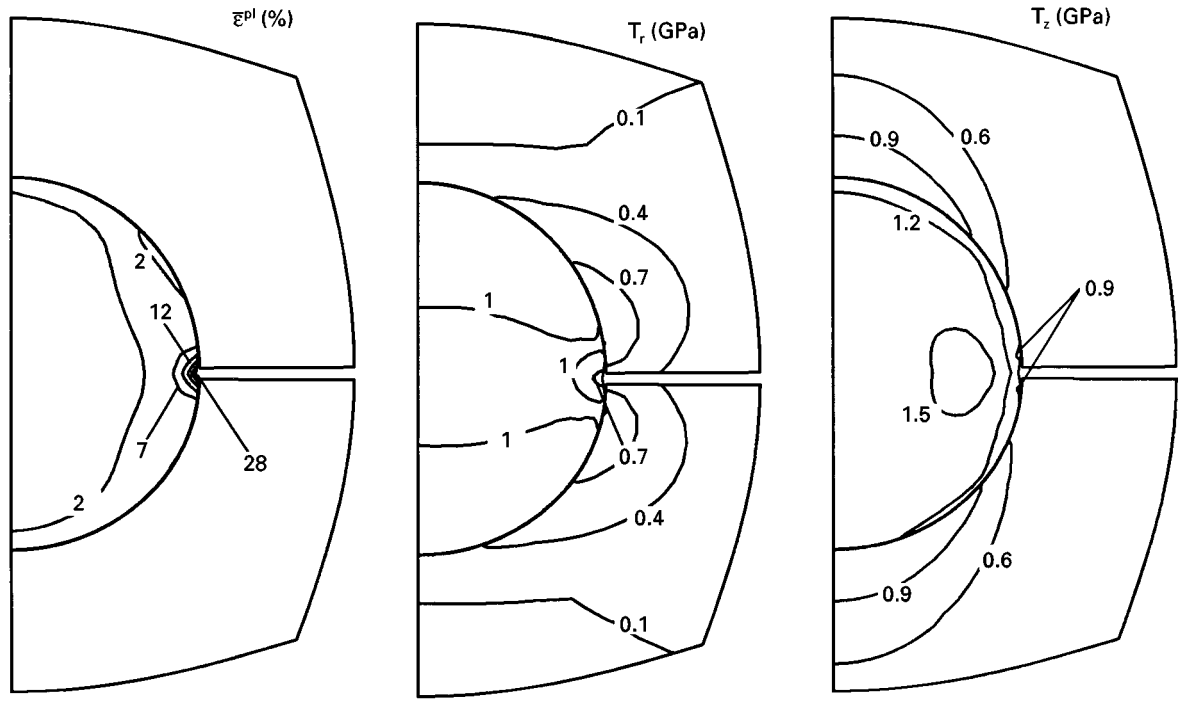

Figure 14 Contour plots of the per cent equivalent plastic strain, (a), radial (b), and axial stress (c), for case D of the β-phase material constitutive relation.

high. This type of materials behaviour is encountered in the case of a metastable β-phase in which plastic deformation is initiated at relatively small stress levels by the activation of a stress-assisted martensitic transformation. As deformation proceeds, however, the high level of hardness of the transformation product (martensite) gives rise to a high rate of strain hardening.

Acknowledgements

The work presented here has been supported by the National Science Foundation under Grants DMR-9317804 and CMS-9531930 and the US Army Research Office, Grant DAAH04-96-1-0197. The authors are indebted to Drs Bruce A. MacDonald and William A. Spitzig of NSF and Dr Wilbur C. Simmons of ARO for continuing interest in the present work. The help of Professor D. Parks of MIT for sharing the unpublished results with us are greatly appreciated.

Appendix

A.1. Determination of the material Jacobian for metastable β-phase

The material Jacobian, $\boldsymbol{J}$ is a fourth-order tensor that represents the rate of change in the increment of the Kirchhoff stress, $\Delta\mathbf{T}$, with respect to a virtual change in the increment in strain, $\Delta\varepsilon$. Thus

$$\boldsymbol{J} = \frac{\mathrm{d}\Delta\mathbf{T}}{\mathrm{d}\Delta\varepsilon} \tag{A1}$$

A detailed derivation of the final form of the Jacobian, as carried out by Zavaliangos and Anand [23], showed that the general form of the material Jacobian can be expressed as

$$\boldsymbol{J} = \mathrm{C}_1\,\mathbf{I} + C_2\,\mathbf{I}\otimes\mathbf{I} + \mathrm{C}_3\,\mathbf{N}\otimes\mathbf{N} + \mathrm{C}_4\,\mathbf{N}\otimes\mathbf{I} + \mathrm{C}_5\,\mathbf{I}\otimes\mathbf{N} \tag{A2}$$

Constants C_1 through C_5 are given by

$$\mathrm{C}_1 = 2\tilde{G} \tag{A3}$$

$$\mathrm{C}_2 = Bd_{22} - \tfrac{1}{3}\,C_1 \tag{A4}$$

$$\mathrm{C}_3 = 2Gd_{11} - \mathrm{C}_1 \tag{A5}$$

$$\mathrm{C}_4 = -2Gd_{21} \tag{A6}$$

$$\mathrm{C}_5 = -Bd_{12} \tag{A7}$$

where

$$\tilde{G} = G\,\frac{\|\,\mathbf{T}'\,\|}{\|\,\mathbf{T}'_{\mathbf{T}}\,\|} \tag{A.8}$$

$$d_{11} = \frac{\partial\,\|\,\mathbf{T}'\,\|}{\partial\,\|\,\mathbf{T}'_{\mathbf{T}}\,\|} \tag{A.9}$$

$$d_{12} = \frac{\partial\ [(1/2)^{1/2}\,\|\,\mathbf{T}'_{\mathbf{T}}\,\|]}{\partial\ [-(1/3)\ \mathrm{tr}\ (\mathbf{T}_{\mathbf{T}})]} \tag{A10}$$

$$d_{21} = \frac{\partial\ [-(1/3)\ \mathrm{tr}\ (\mathbf{T})]}{\partial\ [(1/2)^{1/2}\,\|\,\mathbf{T}'_{\mathbf{T}})]} \tag{A11}$$

$$d_{22} = \frac{\partial\,\mathrm{tr}\,(\mathbf{T})}{\partial\,\mathrm{tr}\,(\mathbf{T}_{\mathbf{T}})} \tag{A12}$$

Differentiation of Equation 32 yields

$$\frac{\partial\ \|\,\mathbf{T}'\,\|}{\partial\ \|\,\mathbf{T}'_{\mathbf{T}}\,\|} = 1 - 6^{1/2}\,G\,\frac{\partial\lambda}{\partial\,\|\,\mathbf{T}'_{\mathbf{T}}\,\|} \tag{A13}$$

$$\frac{\partial\ \|\,\mathbf{T}'\,\|}{\partial\,\mathrm{tr}\ \ \|\,\mathbf{T}_{\mathbf{T}}\,\|} = -6^{1/2}\,G\,\frac{\partial\lambda}{\partial\,\mathrm{tr}\,\|\,\mathbf{T}_{\mathbf{T}}\,\|} \tag{A14}$$

while differentiation of Equation 33 yields

$$\frac{\partial \operatorname{tr}(\mathbf{T})}{\partial \| \mathbf{T}'_{\mathbf{T}} \|} = -3c \frac{\partial \lambda}{\partial \| \mathbf{T}'_{\mathbf{T}} \|} \tag{A15}$$

$$\frac{\partial \operatorname{tr}(\mathbf{T})}{\partial \operatorname{tr}(\mathbf{T}_{\mathbf{T}} \|} = 1 - 3c \frac{\partial \lambda}{\partial \operatorname{tr} \| \mathbf{T}_{\mathbf{T}} \|} \tag{A16}$$

It is clear by analysis, Equations A3–A16, that the constants $C_1 - C_5$ can be determined provided the derivatives $\partial\lambda/\partial \| \mathbf{T}'_{\mathbf{T}} \|$ and $\partial\lambda/\partial \operatorname{tr}(\mathbf{T}_{\mathbf{T}})$ are evaluated. The two derivatives are evaluated as follows.

If the yield potential, Ψ, is defined using Equation 29 as

$$\begin{aligned}\Psi(\| \mathbf{T}' \|, \operatorname{tr}(\mathbf{T}_{\mathbf{T}}), \lambda) &= R(\bar{\varepsilon}_0 + \lambda) - 3/2^{1/2} [\| \mathbf{T}'_{\mathbf{T}} \| - 6^{1/2} G\lambda] \\ &\quad - k[\tfrac{1}{3} \operatorname{tr}(\mathbf{T}_{\mathbf{T}}) - c\lambda] = 0\end{aligned} \tag{A17}$$

then its derivation yields

$$\frac{\partial \Psi}{\partial \| \mathbf{T}'_{\mathbf{T}} \|} + \frac{\partial \Psi}{\partial \lambda} \frac{\partial \lambda}{\partial \| \mathbf{T}'_{\mathbf{T}} \|} = \frac{\partial R}{\partial \lambda} \frac{\partial \lambda}{\partial \| \mathbf{T}'_{\mathbf{T}} \|} - \tfrac{3}{2}^{1/2} \left[1 - 6^{1/2} G \frac{\partial \lambda}{\partial \| \mathbf{T}'_{\mathbf{T}} \|}\right] + kc \frac{\partial \lambda}{\partial \| \mathbf{T}'_{\mathbf{T}} \|} = 0 \tag{A18}$$

$$\frac{\partial \Psi}{\partial \operatorname{tr}(\mathbf{T}'_{\mathbf{T}})} + \frac{\partial \Psi}{\partial \lambda} \frac{\partial \lambda}{\partial \operatorname{tr}(\mathbf{T}_{\mathbf{T}})} = \frac{\partial R}{\partial \lambda} \frac{\partial \lambda}{\partial \operatorname{tr}(\mathbf{T}_{\mathbf{T}})} + 3G \frac{\partial \lambda}{\partial \operatorname{tr}(\mathbf{T}_{\mathbf{T}})} - k\left[\frac{1}{3} - c \frac{\partial \lambda}{\partial \operatorname{tr}(\mathbf{T}_{\mathbf{T}})}\right] = 0 \tag{A19}$$

where

$$h = \frac{\partial R}{\partial \lambda} \tag{A20}$$

After differentiating Equation A17 with respect to $\| \mathbf{T}'_{\mathbf{T}} \|$, $\operatorname{tr}(\mathbf{T}_{\mathbf{T}})$ and λ, Equations A18 and A19 can be solved to yield

$$\frac{\partial \lambda}{\partial \| \mathbf{T}'_{\mathbf{T}} \|} = \frac{(3/2)^{1/2}}{h + kc + 3G} \tag{A21}$$

$$\frac{\partial \lambda}{\partial \operatorname{tr}(\mathbf{T}_{\mathbf{T}})} = \frac{k/3}{h + kc + 3G} \tag{A22}$$

Finally the material Jacobian coefficients C_1–C_5 are evaluated by combining Equations A3–A16, A21 and A22 as

$$C_1 = 2G \frac{\| \mathbf{T}' \|}{\| \mathbf{T}'_{\mathbf{T}} \|} \tag{A23}$$

$$C_2 = B - \frac{Bkc}{h + kc + 3G} - \frac{2G}{3} \frac{\| \mathbf{T}' \|}{\| \mathbf{T}'_{\mathbf{T}} \|} \tag{A24}$$

$$C_3 = 2G \frac{h + kc}{h + kc + 3G} - 2G \frac{\| \mathbf{T}' \|}{\| \mathbf{T}'_{\mathbf{T}} \|} \tag{A25}$$

$$C_4 = -\frac{3^{1/2} Gc}{h + kc + 3G} \tag{A26}$$

$$C_5 = -\frac{3^{1/2} GBk}{h + kc + 3G} \tag{A27}$$

To facilitate numerical calculations, the fourth-order tensor given by Equation A2 should be converted into a (6×6) matrix or into a (4×4) matrix for a plain stress–strain or an axisymmetric analysis.

References

1. L. S. SIGL and H. E. EXNER, *Metall. Trans.* **18A** (1987) 1299.
2. M. S. NEWKIRK, A. W. URQHART and H. R. ZWICKER, *J. Mater. Res.* **1** (1986) 81.
3. I. AKSAY and A. PYSIK, "Ceramic microstructures: role of interfaces, edited by J. A. Pask and A. G. Evans, (Plenum Press, New York, 1987).
4. A. G. EVANS and R. M. MCMEEKING, *Acta Metall.* **34** (1986) 2435.
5. B. BUDIANSKY, J. AMAZIGO and A. G. EVANS, *J. Mech. Phys. Solids* **26** (1989) 364.
6. B. BUDIANSKY, Micromechanics II, Proceedings of the Tenth US Congress on Applied Mechanics (1986).
7. A. G. EVANS and R. M. CANNON, *Acta Metall.* **34** (1986) 761.
8. G. B. OLSON, in "Innovations in ultra-high strength steel technology", edited by G. B. Olson and E. S. Wright, 3rd Sagamore Army Materials Research Conference, Lake George, NY August 30–September 3 (1987) p. 3.
9. M. GRUJICIC and P. DANG, *Mater. Sci. Engng* **A224** (1997) 187.
10. M. GRUJICIC and N. SANKARAN, *Int. J. Solids Struct.* **34** (1997) 4421.
11. *Idem*, *ibid* **83** (1997) 337.
12. A. NEEDLEMAN, *J. Appl. Mech.* **54** (1987) 525.
13. R. E. CECH and D. TURNBULL, *Trans. AIME* **206** (1956) 124.
14. ABAQUS Theory Manual, Verson 5.4, Hibbitt, Karlsson and Sorensen, Inc., Providence, RI (1995).
15. M. GRUJICIC and S. G. LAI, *J. Mater. Sci.* This is Part I, JM 70879.
16. G. BOZZOLO, J. FERRANTE and J. R. SMITH, *Scripta Metall. Mater.* **25** (1991) 1927.
17. X.-P XU and A. NEEDLEMAN, *Modeling Simul. Mater. Sci Engng* **1** (1993) 111.
18. S. SOCRATE, PhD thesis MIT, Cambridge, MA (1996).
19. R. D. KREIG and D. B. KREIG, *J. Pressure Vessel Technol. ASME* **99** (1977) 510.
20. Y.-W. KIM and S. KRISHNAMURTHY, *J. Metals* **43** (1991) 149.
21. L. E. MURR, K. P. STAUDHAMMER and S. S. KECKER, *Metall. Trans.* **13A** (1982) 627.
22. H. CONRAD and R. JONES, in "The science, technology and application of titanium", edited by R. I. Jaffe and N. E. Promisel (Pergamon Press, 1970). pp. 81–501.
23. A. ZAVALIANGOS and L. ANAND, *Int. J. Num. Mech. Engng* **19** (1990) 267.

Received 6 October 1997
and accepted 11 May 1998